Chemical Engineering Journal 453 (2023) 139824

Contents lists available at ScienceDirect

Chemical Engineering Journal

journal homepage: www.elsevier.com/locate/cej

Highly-sensitive volatile organic compounds evaluation by three-dimensional $ZnFe_2O_4/ZnSnO_3$ heterostructures and their predictive grain quality monitoring

Kewei Liu [a], Zichen Zheng [a], Marc Debliquy [b], Chao Zhang [a,*]

[a] College of Mechanical Engineering, Yangzhou University, Yangzhou 225127, PR China
[b] Service de Science des Matériaux, Faculté Polytechnique, Université de Mons, Mons 7000, Belgium

ARTICLE INFO

Keywords:
Gas sensor
1-Octen-3-ol
Rice mildew
Nanocomposite
Heterojunction

ABSTRACT

As a common metabolite of various agricultural products, 1-octen-3-ol plays a key role in cereal quality evaluation with adverse impacts on human health after inhalation, of which the detectors meeting the detection limit of ppb level that satisfies the request of application have been reported rarely. Herein, $ZnFe_2O_4$ and $ZnSnO_3$ are selected to design heterostructured materials for highly sensitive and selective detection of 1-octen-3-ol gas. The sensing results prove that fine-tuned surface oxygen vacancies and highly-efficient electron transition of the nanocomposites are achieved through modulating the loading amount of $ZnFe_2O_4$, contributing to the significantly enhanced response (40.15 @ 50 ppm), low limit of detection (420 ppb), optimized selectivity and excellent long-term stability (40.786 ± 1.693 @ 50 ppm for 15 days). The enhancement mechanism is explained by a large specific surface area with hollow mesoporous structures, consequent bandgap narrowing and decreased charge transfer resistance, which is further verified through DFT analysis. Moreover, the practical application for the unhusked rice detection is carried out. This work shed light on a new promising candidate for detecting characterized volatile organic compounds released from mildewed rice which may strikingly affect the rice storage industry by simplifying the quality control approach to a great extent.

1. Introduction

Rice (Oryza sativa L.) is cultivated on 150 million hectares worldwide, with total production amounting to 600 million tons, accounting for 20 % of all grains. Newly harvested rice is often dried and stored for a long time without shelling to preserve the fresh taste. However, the climate of the place of origin and reserve area of unhusked rice usually undergoes high humidity with a long sweltering summer, and the long-distance transport is always accompanied by muggy conditions, which provide a suitable environment for the mold to multiply [1]. The mildew process of stored rice is inevitable even under stringent storage methods. Once the mildewed rice enters the circulation market, it will generate a series of toxic side-effects such as cytotoxicity, reproductive toxicity, immunotoxicity, genotoxicity, hepatotoxicity and nephrotoxicity, etc., eventually causing serious hidden dangers to people and livestock health. Therefore, how to detect effectively whether rice is moldy has become essential work to ensure food security. Conventional artificial qualitative analysis has a lack of predictability and is obviously subjective, prone to place observers at serious risk of respiratory disease, which has remained controversial. Besides, commonly reported laboratory off-line testing is destructive, time-consuming and hardly implement real-time monitoring, which is only applicable after discernible fungi growth appears in an advanced period of biodeterioration [2,3]. Fatty acid value, gelatinization characteristics, germination percentage, electrical conductivity, morphology, color and odor are the dominated evaluation indexes in current studies, among which nondestructive odor detection via gas sensor has been reported minimally [4]. Accompanying the rice mildew process is unpleasant volatile organic compounds (VOCs) which easily draw people's attention, while in the early stage of mildew, the changes in odor are too subtle to notice. It implies that by the time the peculiar smell of mildew is perceived by people, rice has been contaminated by vast quantities of mold and lost edible value. In various VOCs released from rice mildew, mushroom-scented 1-octen-3-ol, as unsaturated alcohol derived from 10-hydroperoxide of linoleic acid, is deemed to be a characteristic flavor component generated from fungi with a low odor threshold [5,6], of which the

* Corresponding author.
E-mail address: zhangc@yzu.edu.cn (C. Zhang).

https://doi.org/10.1016/j.cej.2022.139824
Received 10 August 2022; Received in revised form 5 October 2022; Accepted 12 October 2022
Available online 17 October 2022

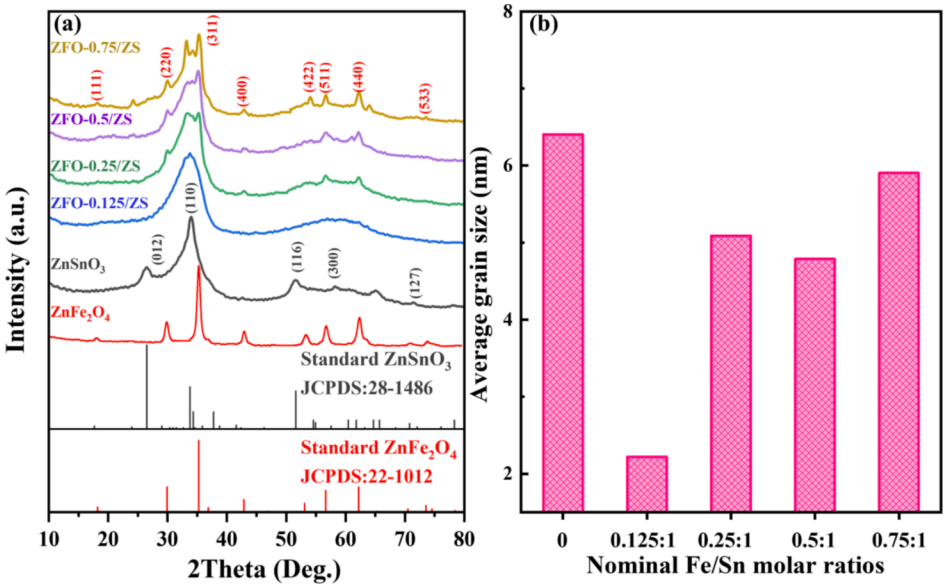

Fig. 1. (a) XRD patterns and (b) average grain sizes of all samples.

contents rise constantly during rice storage. However, even though 1-octen-3-ol is a common metabolite of diverse molds, no specific materials or research approaches have been reported for detecting it released from stored rice. There are few studies on the gas sensing performance for monitoring 1-octen-3-ol, and the limit of detection (LOD) reaches tens of ppm, which hardly meets the requirements of accurate evaluation of early rice mildew at even ppb level [7]. Besides, 1-octen-3-ol has been known as characteristic volatile in other agricultural products and demonstrated to act as an insect attractant, induce disease resistance of fruit and prompt human embryonic stem cells to exhibit more cytotoxicity, highlighting its great research value in rapid and real-time detection at low concentrations [8–12].

Ternary oxide semiconductor $ZnSnO_3$, as a thermal decomposition product of $ZnSn(OH)_6$, is a kind of non-centrosymmetric oxide with perovskite structure (ABO_3) [13], of which the structural stability is commonly characterized through Goldschmidt tolerance factor, defined as $t = \frac{r_A+r_O}{\sqrt{2}(r_B+r_O)}$, where r reparents ionic radius. The calculated value t of $ZnSnO_3$ is less than 0.9, which means the crystal structure is not an ideal octahedron and is prone to occur oxygen octahedral distortion [14]. Besides, $LiNbO_3$-type and ilmenite-type $ZnSnO_3$ have also been explored extensively [15–18]. For orthonormal perovskite $ZnSnO_3$, SnO_6 octahedrons tend to rotate and tilt. Because of the smaller radius of O atom, the defects tend to form when there are external factors such as pressure, doping and temperature. In order to maintain structural stability, O^{2-} will leave its previous junction with the metal ion because the amphoteric ions of Zn^{2+} and Sn^{4+} are easily dissolved in an alkaline solution, resulting in the formation of oxygen defects [19]. Such defects significantly contribute to the production of oxygen vacancies and chemisorbed oxygen on the material surface, which act as donors when exposed to reducing gases, thus enhancing the sensing performance. There has been growing interest in advance of $ZnSnO_3$ based real-time sensing platforms for VOCs [20–26]. Transition metal oxides, e.g., spinel ferrites (AB_2O_4), have recently emerged as a kind of worthwhile research materials for gas sensing, ascribing to their unique regular crystal structure and rich defects [27,28]. Each unit cell of *n*-type face-centered cubic $ZnFe_2O_4$ contains 56 ions, closely packed by 32 oxygen anions to form tetrahedral interstices occupied by Zn^{2+} and octahedral interstices occupied by Fe^{3+}. The cations only account for a quarter of the total interstices, which contributes to the formation of oxygen vacancies. The strong tendency of Zn^{2+} for occupation maintains the typical spinel structure [29]. Besides, $ZnFe_2O_4$ exhibited excellent selectivity and sensitivity to reducing gas [30–32]. Superior VOCs gas sensor based on micro-nano structured $ZnFe_2O_4$ has attracted much attention recently [33–36].

Optimizing response while minimizing response/recovery time requires expanding single-component sensing material to multi-component heterostructure to construct adjustable chemical compositions and realize synergistic effects, which has been widely applied [37–39]. The purpose is to fabricate ultrasensitive materials with redistributed charges that possess properties superior to all properties of constituent parts. $ZnSnO_3$ with a wide bandgap width (~3.7 eV) is usually used as backbone material, which combines with narrow bandgap semiconductor $ZnFe_2O_4$ (~1.9 eV) to establish *n-n* heterostructure, restricting the recombination of the carriers and enhancing their transportation [40,41].

Herein, we reported the $ZnSnO_3$ nanocubes loaded with a small amount of $ZnFe_2O_4$ nanoparticles contributed to the ultrasensitive sensing performance based on *n-n* heterostructure with a combination of low LOD (420 ppb), high response (~41), short response/recovery time (~128 s/~100 s) for 50 ppm 1-octen-3-ol. Density functional theory (DFT) calculations were conducted to expound on the strengthened sensing mechanism. Moreover, the application in early mildew conditions of unhusked rice was studied to verify its practicality. The results provided a new promising candidate for detecting characterized VOCs released from early mildewed rice, which may positively affect the rice storage industry by simplifying the quality control strategy to a large extent.

2. Experimental section

The details of raw materials, synthetic process and test equipment are provided in Supporting information. $ZnFe_2O_4/ZnSnO_3$ heterojunction structures were prepared via a simple two-step strategy. The nominal Fe/Sn molar ratios of 0.125:1, 0.25:1, 0.5 and 0.75:1 are denoted as ZFO-x/ZS (x = 0.125, 0.25, 0.5 and 0.75). The as-synthesized powders (~2 mg) were first blended with deionized water (~1 mL) to ground into a homogeneous slurry and then directly coated onto sensor substrates patterned with interdigitated Pt electrodes. The obtained sensors for follow-up experiment were heated in an oven at 80 °C for 12 h, as shown in Fig. S1, from which it was easy to observe that the color of sensing layer became darker with the increase of $ZnFe_2O_4$ loading amount. Figs. S1 and S2 display the home-built testing system with a 4-channel gas sensing measuring equipment (Wuhan Huachuang Ruike

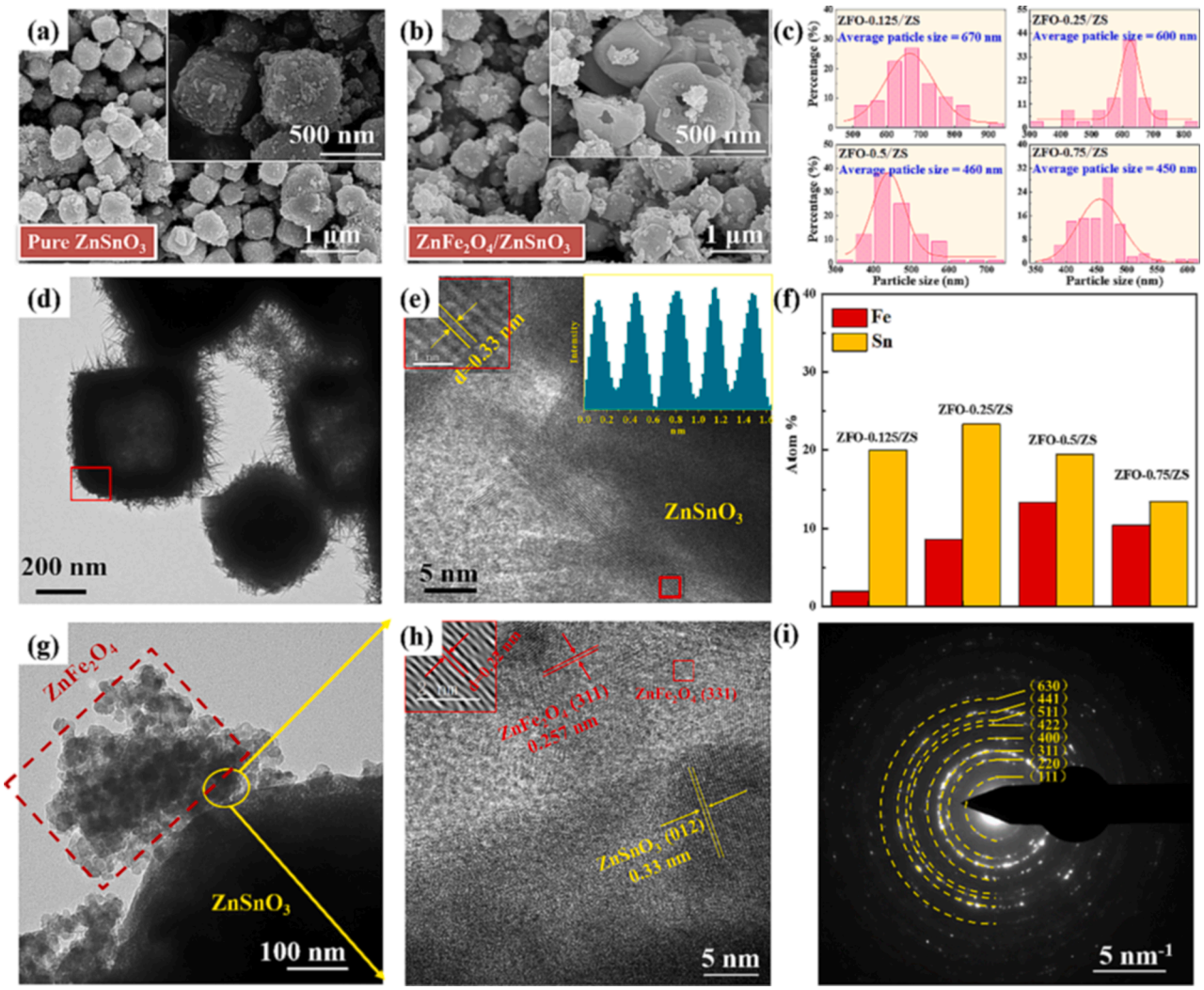

Fig. 2. Structural characterization of pure $ZnSnO_3$ and $ZnFe_2O_4/ZnSnO_3$. (a-b) FESEM images of pure $ZnSnO_3$ and $ZnFe_2O_4$-0.5/$ZnSnO_3$ nanocubes. Inset: their high-magnification images. (c) Particle distribution histograms of the $ZnFe_2O_4$-(0.125, 0.25, 0.5, 0.75)/$ZnSnO_3$ with more than 100 nanocubes measured. (d, g) TEM and (e, h) HRTEM images of $ZnSnO_3$ and $ZnFe_2O_4$-0.5/$ZnSnO_3$ at different magnifications by drop-casting suspension on TEM grids and drying in air. The crystallites in the images are color-coded according to their lattice fringes: the (012) plane of orthorhombic $ZnSnO_3$; the (311) and (331) planes of cubic $ZnFe_2O_4$. Inset: Intensity profiles of $ZnSnO_3$ in the marked area in (e) in panel. (f) Atomic ratios of Fe and Sn in $ZnFe_2O_4$-(0.125, 0.25, 0.5, 0.75)/$ZnSnO_3$ through EDS spectra. (i) SAED image of and cubic $ZnFe_2O_4$ loaded on and $ZnFe_2O_4$-0.5/$ZnSnO_3$.

Technology Co., Ltd.) operated at 18.7 V and 0.34 A with a DC supply, which can provide real-time electrical resistance signals. Three mass flow controllers (Bronkhorst, Germany) were utilized to precisely regulate and mix the concentrations of target gases. The liquid VOCs passed into gas chamber by using high purity air (79 % N_2 + 21 % O_2) as carrier gas. Fig. S3 illustrates the measurement system for rice mildew detection. The total flow rate was set to 500 mL/min. Purchased unhusked rice was naturally stored in the barn for 3 months and then treated at 50 °C with 80 % relative humidity (RH) for various durations (3, 7, 10, and 30 days). The 1-octen-3-ol concentrations corresponding to stored rice were calculated to study the mildew degree further.

Here, the *n*-type response was defined as Ra/Rg, in which Ra and Rg represent the stable resistance values of gas sensor after exposure to air and mixed gases. The response/recovery time (τ_{res}/τ_{rec}) is estimated as the time taken by the sensor to achieve 90 % of the total resistance change in the case of adsorption and desorption process.

3. Results and discussion

3.1. Characterization results

Fig. 1a exhibits the phase composition and purity of as-prepared samples. The diffraction peaks of pure $ZnSnO_3$ and $ZnFe_2O_4$ are in accord with orthorhombic structured $ZnSnO_3$ standard card (JCPDS: 28-1486) and bulk cubic spinel-structured $ZnFe_2O_4$ standard card (JCPDS: 22-1012), respectively. No other impurity peaks were observed. Besides, the XRD pattern of the $ZnSn(OH)_6$ was analyzed to verify the crystal structure of $ZnSnO_3$, because $ZnSnO_3$ was generated by the dehydration of $ZnSn(OH)_6$. As shown in Fig. S4, all the diffraction peaks were well indexed to the standard card (JCPDS: 74–1825), which appeared sharp and narrow in relation to good crystallinity and high purity. Compared to the bulk materials, the peaks of pure $ZnSnO_3$ and their composites were fairly broadened due to the decreased crystal sizes. The intensity of (111), (220), (311), (400), (422), and (440) in ZFO/ZS increased with the growing loading amount of $ZnFe_2O_4$, manifesting the successful preparation of the ZFO/ZS composites. Fig. 1b presents that the nano-grain sizes decreased after loading $ZnFe_2O_4$. The lowered grain size was demonstrated to be driven by the enhancement of free energy of

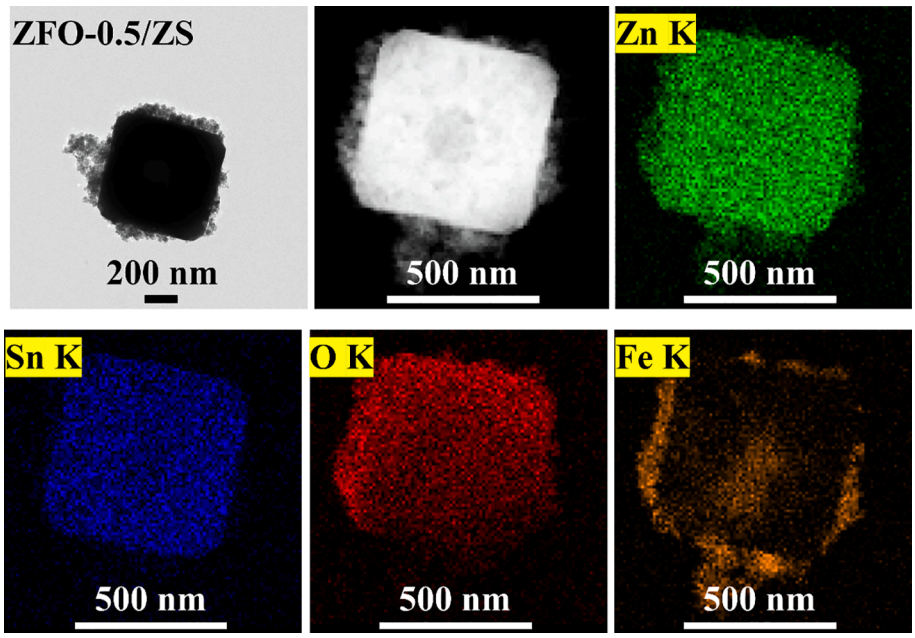

Fig. 3. EDX elemental mapping of $ZnFe_2O_4$-0.5 $ZnSnO_3$.

nanostructure, caused by the increase in the total area of grain boundary and potential barriers among nanograins. The average grain sizes of pure $ZnSnO_3$ and $ZnFe_2O_4$ were calculated to be 6.396 nm and 10.977 nm (Table S1), which were both larger than those of the composites. The broadening of diffraction peaks of the composites represented the decrease in grain sizes, implying the formation of heterostructure. The intensity of diffraction peaks gradually increased with the growth of $ZnFe_2O_4$ loading amount, indicating the ideal co-existence of two phases in the as-synthesized composites. ZFO-0.125/ZS had the smallest grain size, followed by ZFO-0.5/ZS. Notably, the phenomenon that the grain size of ZFO-0.5/ZS was slightly smaller than that of ZFO-0.25/ZS can be explained by more defects generated in ZFO-0.5/ZS, which will change its crystallization degree and lead to the weakening of the intensity of some diffraction peaks in ZFO-0.5/ZS. Moreover, the comparative-limited crystallization will result in a larger peak width and smaller grain size of ZFO-0.5/ZS. Besides, the crystallinity of ZFO-0.5/ZS was clearly higher than that of ZFO-0.125/ZS through the integrated intensity of diffraction peaks, and the grain size was obviously smaller than that of ZFO-0.75/ZS with the highest crystallinity, which means that ZFO-0.5/ZS may possess the best sensing properties consistent with the subsequent gas sensing experiment results [29].

The specific morphologies and microstructures of $ZnSnO_3$ and ZFO/ZS composites were investigated by FESEM, TEM and HRTEM. Fig. 2a illustrates that $ZnSnO_3$ has a good morphological uniformity of cube-like shape, which usually occurs in the fabrication process without adding surfactant. An inset figure demonstrates that the cubes have rough faces with abundant irregular fragments, of which the edges reach around 650 nm. The appearance of relatively coarse surface may be due to the loss of crystal water during calcination. The growing mechanism can be concluded that the decomposition of unstable phase of $ZnSn(OH)_6$ promotes the nucleation and growth of $ZnSnO_3$ nanocrystals, developing further into self-aggregated $ZnSnO_3$ nanoclusters which are stacked into larger cubic nanocrystallites with a few amorphous nanoparticles adhering to the surface during the hydrothermal process. The attached nanoparticles dwindled and the established $ZnSnO_3$ experienced a dissolution–recrystallization process for growing into larger-sized cubes according to Ostwald ripening. Besides, the hollow interior may result from the excessive amount of KOH added as a reactant agent, from which the hydroxyl groups will lead to the complete dissolution of inner $ZnSn(OH)_6$ with smaller size, less dense and high surface energy. As shown in Fig. 2b and g, the cubic $ZnSnO_3$ microstructure was retained with the evolution of cluster-like $ZnFe_2O_4$ anchoring their surfaces and growing outwardly after hydrothermal reaction to form decorative heterostructure, which can also be observed in Figs. S5 and S6. $ZnSnO_3$ remained a hollow structure and Fe element uniformly covered the surface of $ZnSnO_3$ or aggregated around it with different quantities of $ZnFe_2O_4$. With the increase in load amount, the $ZnFe_2O_4$ nanoparticles outside the cubes become denser. It should be noted that Sn element appears almost exclusively on the $ZnSnO_3$ cubes, which is largely absent from the surrounding loading clusters, and Fe element is only observed on the surface. This phenomenon contributes to the formation of dense heterogeneous interfaces and the improvement of the charge transfer ability of the contact interface (Fig. 3). In order to further visually and accurately testify the changes in the load amount of the ZFO/ZS composites, Fig. 2f exhibits an increase in $ZnFe_2O_4$ loading onto $ZnSnO_3$ as evidenced by the atomic ratios of iron and tin gradually approaching. Moreover, it can also be demonstrated by the variation of Fe peak intensity in EDX spectrum (Fig. S6). $ZnFe_2O_4$ showed increasingly apparent cluster morphology, and urchin-like $ZnFe_2O_4$ gathered on the surface of $ZnSnO_3$ when the molar ratio of Fe to Sn reached 0.75, which may be ascribed to positioning self-assembly and Ostwald ripening (Fig. S5). The particle sizes decreased significantly with the increase of load amount, as revealed in Fig. 2c, primarily because the binding action established between $ZnSnO_3$ and $ZnFe_2O_4$ restrained the continuous growth of $ZnSnO_3$ cubes and eventually decreased the particle sizes [26]. The smaller-sized particles will contribute to the sensing properties. As evident in Fig. 2d, there exists obvious light and shade contrast between the inner area and the outer shell, which proves that the $ZnSnO_3$ possesses a hollow structure with a shell thickness of about 100 nm. Besides, fragments aggregate on the surface turned out to be villous nanorods oriented in random directions. The spaces between lattice fringes with the good two-dimensional resolution are equal to the interplanar spacing of the lattice planes, of which the size represents different crystal faces. In Fig. 2e and 2 h, the crystal lattice fringes are clearly visible, indicating the $ZnSnO_3$ and their composites are in a highly crystallized state, which was measured to be 0.33 nm, closely matching the interplane spacing of (0 1 2) lattice plane of $ZnSnO_3$, 0.22 nm and 0.257 nm in good agreement with the (3 3 1) and (3 1 1) lattice planes of $ZnFe_2O_4$ [42]. The SAED result demonstrates that $ZnFe_2O_4$ nanoparticles have a single pure phase without any other phase (Fig. 2i).

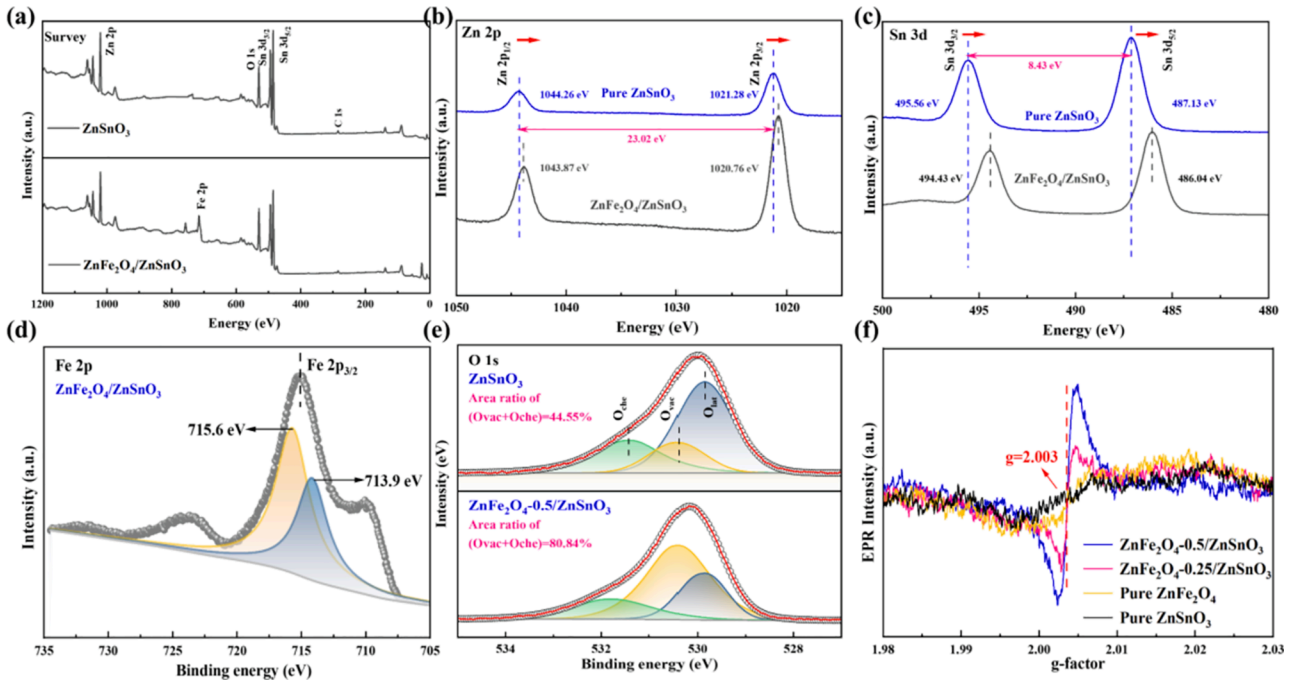

Fig. 4. (a–e) XPS spectra of pure $ZnSnO_3$ and $ZnFe_2O_4$-0.5/$ZnSnO_3$: survey, Zn 2p, Sn 3d, Fe 2p and O 1s. (f) EPR spectra of pure $ZnSnO_3$, pure $ZnFe_2O_4$, $ZnFe_2O_4$-0.25/$ZnSnO_3$ and $ZnFe_2O_4$-0.5/$ZnSnO_3$.

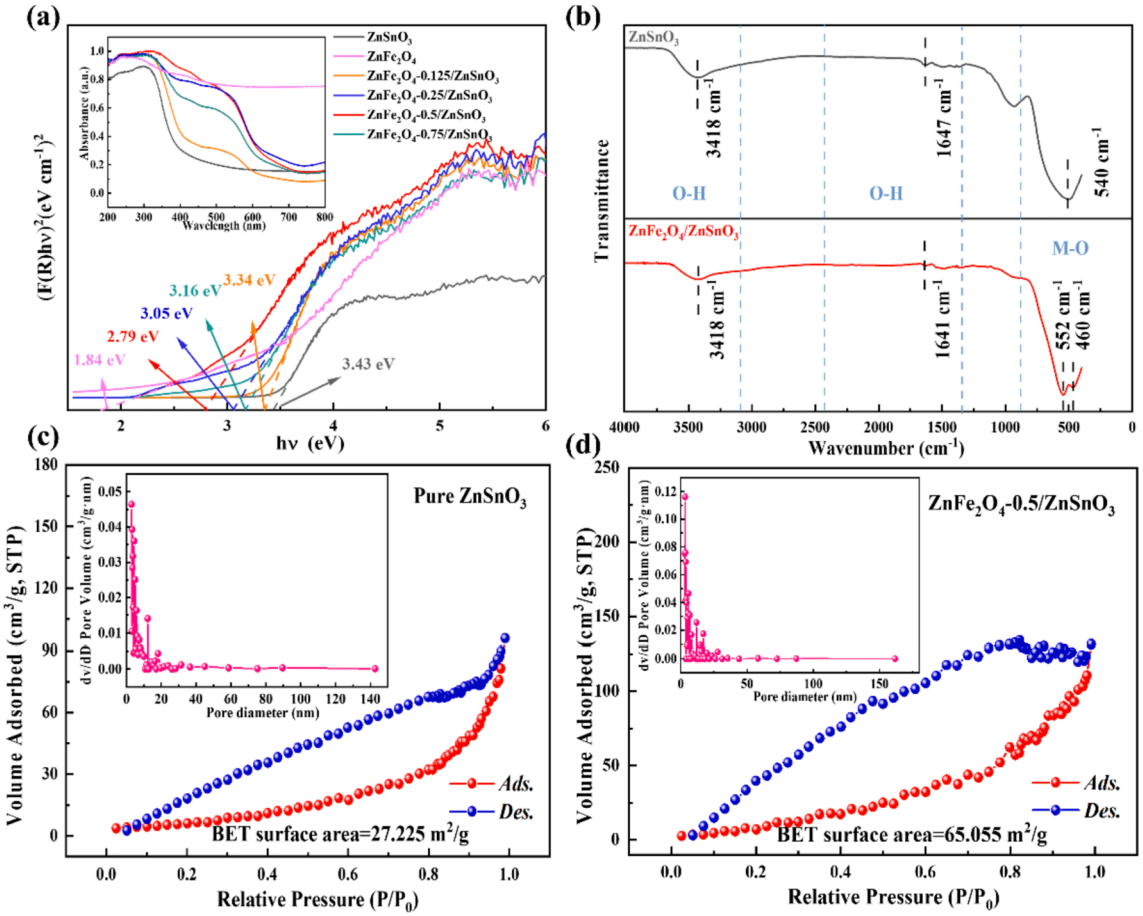

Fig. 5. (a) Plots of $(\alpha h\nu)^2$ versus $h\nu$ of different composite samples. Inset: UV–vis DRS spectrum. (b) FT-IR spectrum of pure $ZnSnO_3$ and $ZnFe_2O_4$-0.5/$ZnSnO_3$. (c-d) Nitrogen adsorption–desorption isotherms (Inset: BJH pore volume distribution curves) of pure $ZnSnO_3$ and $ZnFe_2O_4$-0.5/$ZnSnO_3$.

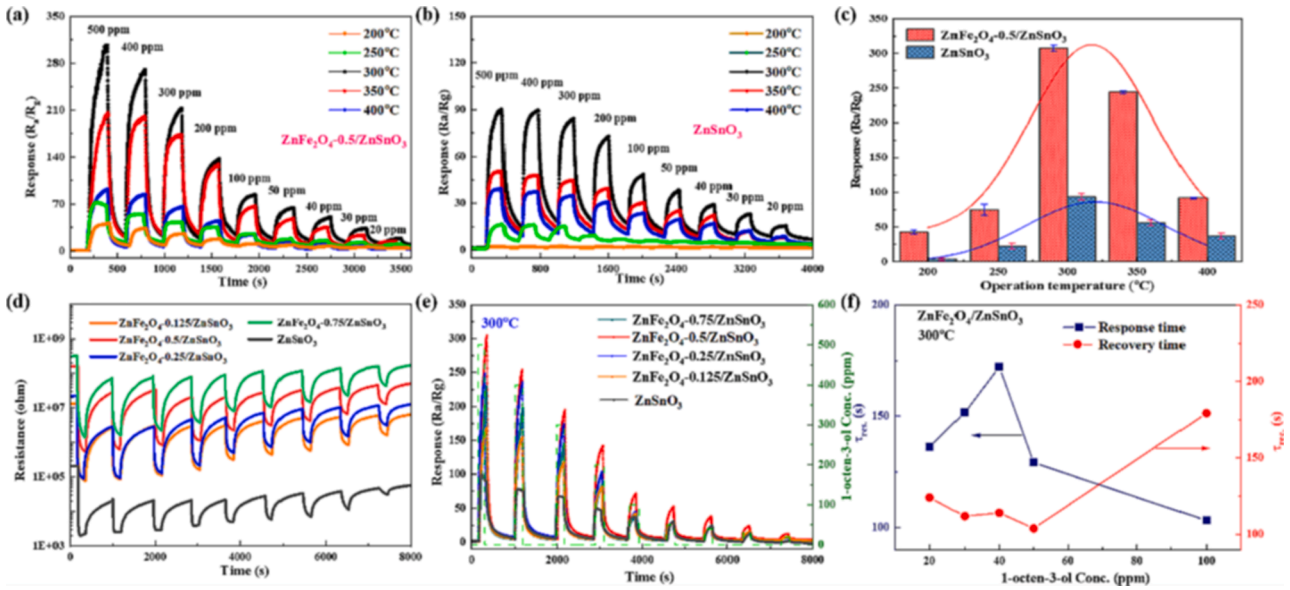

Fig. 6. (a-b) Dynamic response-recovery curves of pure $ZnSnO_3$ and $ZnFe_2O_4$-0.5/$ZnSnO_3$ to 500–20 ppm 1-octen-3-ol at various operation temperatures ranging from 200 °C to 400 °C. (c) The average responses of pure $ZnSnO_3$ and $ZnFe_2O_4$-0.5/$ZnSnO_3$ for 500 ppm 1-octen-3-ol at different temperatures. The error bars represent the standard deviations of three repeated test results. (d-e) The dynamic resistance curves and response-recovery curves of pure $ZnSnO_3$ and $ZnFe_2O_4$-(0.125, 0.25, 0.5, 0.75)/$ZnSnO_3$ to 500–20 ppm 1-octen-3-ol at their optimum operating temperature of 300 °C. (f) The response-recovery times of $ZnFe_2O_4$-0.5/$ZnSnO_3$ as a function of 1-octen-3-ol concentrations ranging from 20 ppm to 100 ppm at 300 °C.

A range of concentric rings connected by vast bright spots could be obviously recognized, proving that the as-synthesized $ZnFe_2O_4$ is a typical polycrystalline material. The calibrated electron diffraction rings from inside to outside were consistent with the (111), (220), (311), (400), (422), (511), (441), and (630) crystal planes of $ZnFe_2O_4$, in line with the XRD results.

XPS analysis was conducted to further describe the composition of pure $ZnSnO_3$ and the composites based on ZFO/ZS, as shown in Fig. 4a–e. The full scan spectrum contained Zn, Sn, O elements, and the observable Fe element appeared after loading $ZnFe_2O_4$. In the case of Zn 2p spectrum, the split peaks of $ZnSnO_3$ at 1044.26 eV and 1021.28 eV corresponded to Zn $2p_{1/2}$ and Zn $2p_{3/2}$, respectively, between which the binding energy separation reached 22.98 eV, in line with the Zn^{2+} oxidation state. As shown in Fig. 4c, two strong peaks at 495.56 eV and 487.13 eV were assigned to Sn $3d_{3/2}$ and Sn $3d_{5/2}$, which confirmed the presence of Sn^{4+} ions with the splitting energy of 8.43 eV. Noticeably, the spin-orbits of Zn 2p and Sn 3d of ZFO-0.5/ZS composite slightly moved towards lower binding energies, which means small amounts of electron transfer may occur in the heterojunction region formed between the loaded $ZnFe_2O_4$ and $ZnSnO_3$. Fig. 4d showed that Fe $2p_{3/2}$ could be decomposed into two characterized peaks centering at 713.9 eV and 715.6 eV, ascribed to the tetrahedral and octahedral of Fe^{3+} [26,43]. The magnified spectrum of O 1s can be fitted into three peaks with broad and asymmetric features, as revealed in Fig. 4e and S8a. The binding energies at around 529.8 eV, 530.4 eV, and 531.6 eV were associated with lattice oxygen (O_{lac}), oxygen vacancy (O_{vac}) and chemisorbed oxygen species (O_{che}). The comparative area ratio of O_{vac} and O_{che} constituents was 44.55 % in pristine $ZnSnO_3$, while when the $ZnFe_2O_4$ nanoclusters successfully loaded on its surface, significant rises in area ratios were observed intuitively in Table S2, resulting from less bandgap energy needed for oxygen to capture electrons from the conduction band of the nano heterojunction composites. The highest content of O_{vac} and O_{che} on the surface of ZFO-0.5/ZS, which reached 80.84 %, led to superior sensing performance compared to other samples. The EPR results in Fig. 4f showed that pure $ZnSnO_3$, pure $ZnFe_2O_4$ and their composites possessed paramagnetic transitions at g≈2.003, of which the ZFO-0.5/ZS exhibited the sharper signal, assigned to the highest content of paramagnetic oxygen vacancies. The pristine $ZnSnO_3$ and $ZnFe_2O_4$ exhibited weak signals, which became stronger with the appearance of heterojunctions, representing relatively low oxygen vacancy concentrations existing in both pristine materials. The characteristic of $ZnSnO_3$ crystal structure prone to form oxygen defects with distortion, the replacement of Fe^{3+} with Fe^{2+} in spinel zinc ferrite for attaining charge balance and the construction of heterojunction, which further improved the oxygen vacancy concentration of the composite resulted in the emergence of unpaired free electron in crystal lattice, thus generating EPR signals [44]. Besides, the existence of oxygen vacancies was further investigated through the photoluminescence (PL) system, as shown in Fig. S8b. The visible luminous peak of the composite with a broad emission feature was notably above that of pure $ZnSnO_3$, demonstrating the formation of a considerable concentration of oxygen vacancies.

Ultraviolet–visible diffuse reflectance spectra (UV–vis DRS) was utilized to analyze the band structures of ZFO/ZS composites. Fig. 5a exhibits that all samples have visible-light adsorption and the adsorption capacity increases with the loading of $ZnFe_2O_4$, which may result from the irregular and dispersed loose morphology of the loaded $ZnFe_2O_4$ nanoclusters as shown in SEM images. Compared with pure $ZnSnO_3$ with almost no absorbance for visible light, the absorption edges presented systematic redshift with longer wavelengths accompanied by adding loading amount and an additional broad absorption band exceeding 700 nm appeared, implying the enhanced photo-absorption capability of the $ZnFe_2O_4$ and heterostructures, which may demonstrate new energy levels established below the conduction band of $ZnFe_2O_4$. The absorption of photons with energy close to the bandgap for semiconductors results in an optical transition (hν≈Eg), of which the wave vector is conserved. In this case, semiconductors such as $ZnSnO_3$ and $ZnFe_2O_4$ are called direct bandgap semiconductors. Their composites' optical band gap energies can be estimated to be 2.79 eV, 3.05 eV, 3.16 eV, and 3.34 eV for ZFO-0.5/ZS, ZFO-0.25/ZS, ZFO-0.75/ZS and ZFO-0.125/ZS based on Kubelka-Munk formula (Equation S2-S6). It is acknowledged that the formation of O_{vac} will contribute to shortening the bandgaps of semiconductors, thus improving the electrons transfer efficiency, which was closely bound up with XPS results. The FT-IR profile was observed in Fig. 5b. Peaks of $ZnSnO_3$ at 540 cm^{-1}, 1647 cm^{-1} and 3418 cm^{-1} were ascribed to Sn–O stretching type, O–H bend vibration and water absorbed on the surface after calcination respectively, which were

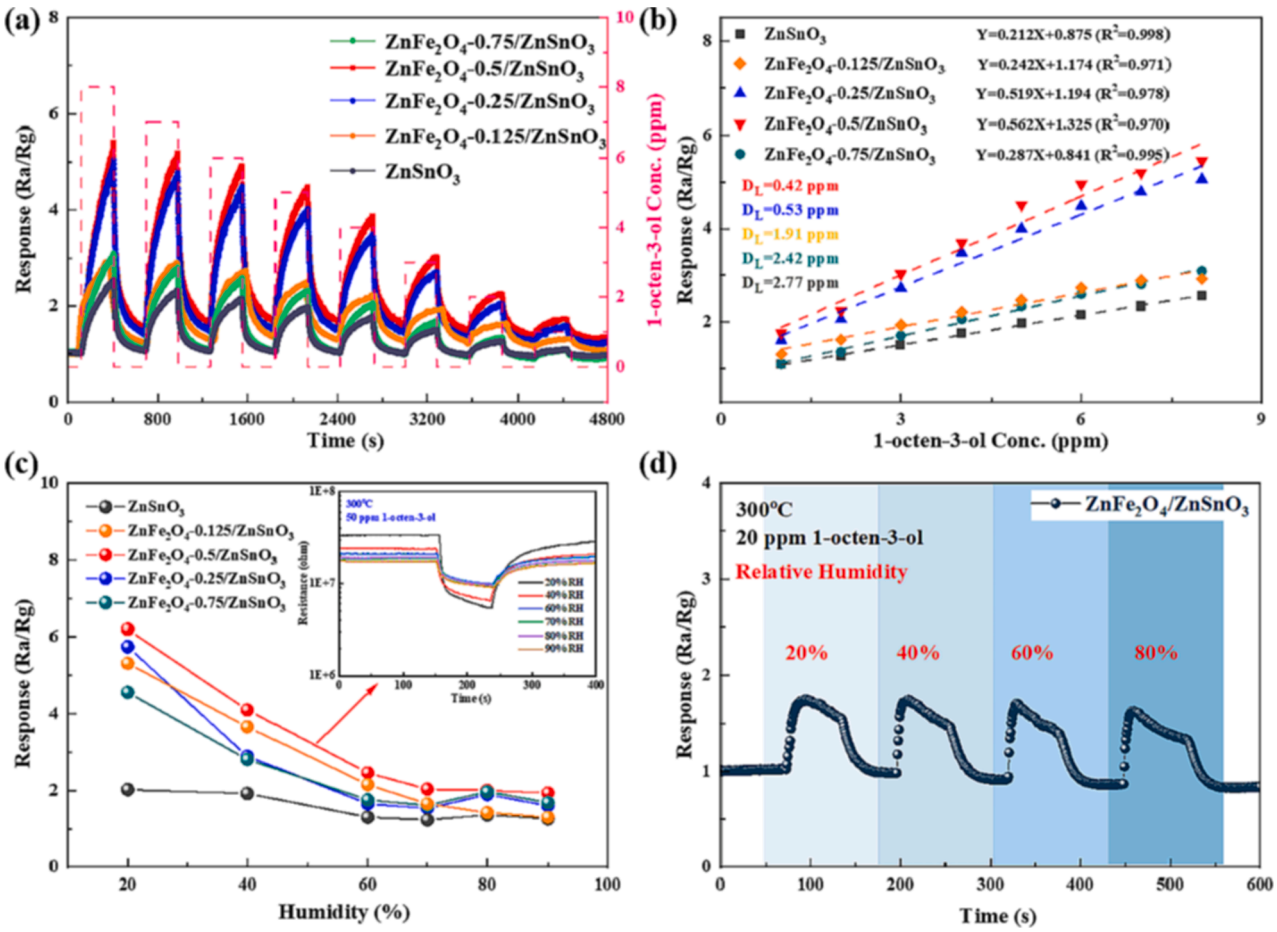

Fig. 7. (a) Transient responses of 8–1 ppm 1-octen-3-ol for pure $ZnSnO_3$ and composites at 300 °C. (b) Linear relationship between response and gas concentration for pure $ZnSnO_3$ and composites and corresponding calculated detection limit. (c) The sensitivity in various relative humidity toward 50 ppm of 1-octen-3-ol. Inset: resistance curves of optimum $ZnFe_2O_4$-0.5/$ZnSnO_3$ in various relative humidity. (d) a real-time response curve of changing relative humidity at 20 ppm 1-octen-3-ol (the resistance stabilized at 20 ppm 1-octen-3-ol was used as the reference resistance).

weaker and less numerous than precursor $ZnSn(OH)_6$ due to its decomposition (Fig. S9a) [45]. After loading $ZnFe_2O_4$, two prominent vibrational peaks of $ZnFe_2O_4$ at 552 cm^{-1} and 460 cm^{-1} were easily observable, according with the vibrations of the octahedral complexes Fe-O and tetrahedral complexes Zn-O [46]. A slight peak offset of the composite may be resulted from the $ZnSnO_3$ as backbone materials. Besides, the Raman spectra in Fig. S9b showed two representative peaks at 540 cm^{-1} and 671 cm^{-1}, corresponding to internal vibration of oxygen tetrahedrons and $ZnSnO_3$ respectively. Others can be assigned to five active Raman modes of $ZnFe_2O_4$ with the space group *Fd*-3m [47,48]. The BET analysis was explored for further examination of specific surface area and pore size distribution of pure $ZnSnO_3$ and their composites. The hysteresis loops in Fig. 5c and d exposed that samples had irregular pore structures. The surface areas of pure $ZnSnO_3$ and ZFO-0.5/ZS reached 27.225 m^2 g and 65.055 m^2 g, the average pore diameters were centered at 2.972 nm and 3.312 nm, and the total pore volumes were situated on 0.148 $cm^3.g^{-1}$ and 0.204 $cm^3.g^{-1}$. The tested data of ZFO-0.125/ZS, ZFO-0.25/ZS, and ZFO-0.75/ZS were listed in Table S3, all samples presented mesopore size distributions (peak pores at circa 2–4 nm), and the specific surface areas (S) evidently increased with diminishing the particle sizes (D) based on the formula $S = 6/D^*\rho$ (ρ represents the crystal density), which conformed to Fig. 2c [49]. The largest total pore volume of ZFO-0.5/ZS was conducive to the diffusion of 1-octen-3-ol, thus enhancing the sensing performance. Besides, the loading of $ZnFe_2O_4$ notably increased the specific surface compared to pristine $ZnSnO_3$. After comparison, the gas sensing performance of ZFO-0.5/ZS was thus expected to be excellent on account of the largest specific surface area and total pore volume of the small-sized particles. The thermostability of pure $ZnSnO_3$ and their composites were also evaluated through TGA (Fig. S9c-d). There was little weight loss appeared over the entire heating process except for the removal of absorbed water, testifying that the as-prepared samples possessed good stability in the heated environment of subsequent gas sensing experiments. The sharp weight loss of $ZnSnO_3$ precursor near 170 °C was attributed to the decomposition of $ZnSn(OH)_6$, which generated $ZnSnO_3$.

3.2. Gas sensing performances

To evaluate the gas sensing performance of the as-fabricated sensors, the working temperature should be prior to research due to its important role in gas sensors. The dynamic response/recovery curves of ZFO-0.5 and pure $ZnSnO_3$ toward 500–20 ppm 1-octen-3-ol at working temperatures within the scope from 200 °C to 400 °C with 50 °C intervals are displayed in Fig. 6a and b. Both samples presented a similar volcano-shape through GaussAmp fitting, which showed the highest response attained at 300 °C (Fig. 6c). The sensors first exhibited a sharp leap in response values with the rise of operating temperature, and then began a smaller decline after reaching the maximum, which was commonly related to the surmounting of activation energy of chemisorption and surface reaction, as the dominant role of desorption in dynamic equilibrium with the further rise of temperature was displayed synchronously [50]. It is noteworthy that the gas sensing performance of the ZFO-0.5/ZS composite was greatly upgraded through loading $ZnFe_2O_4$

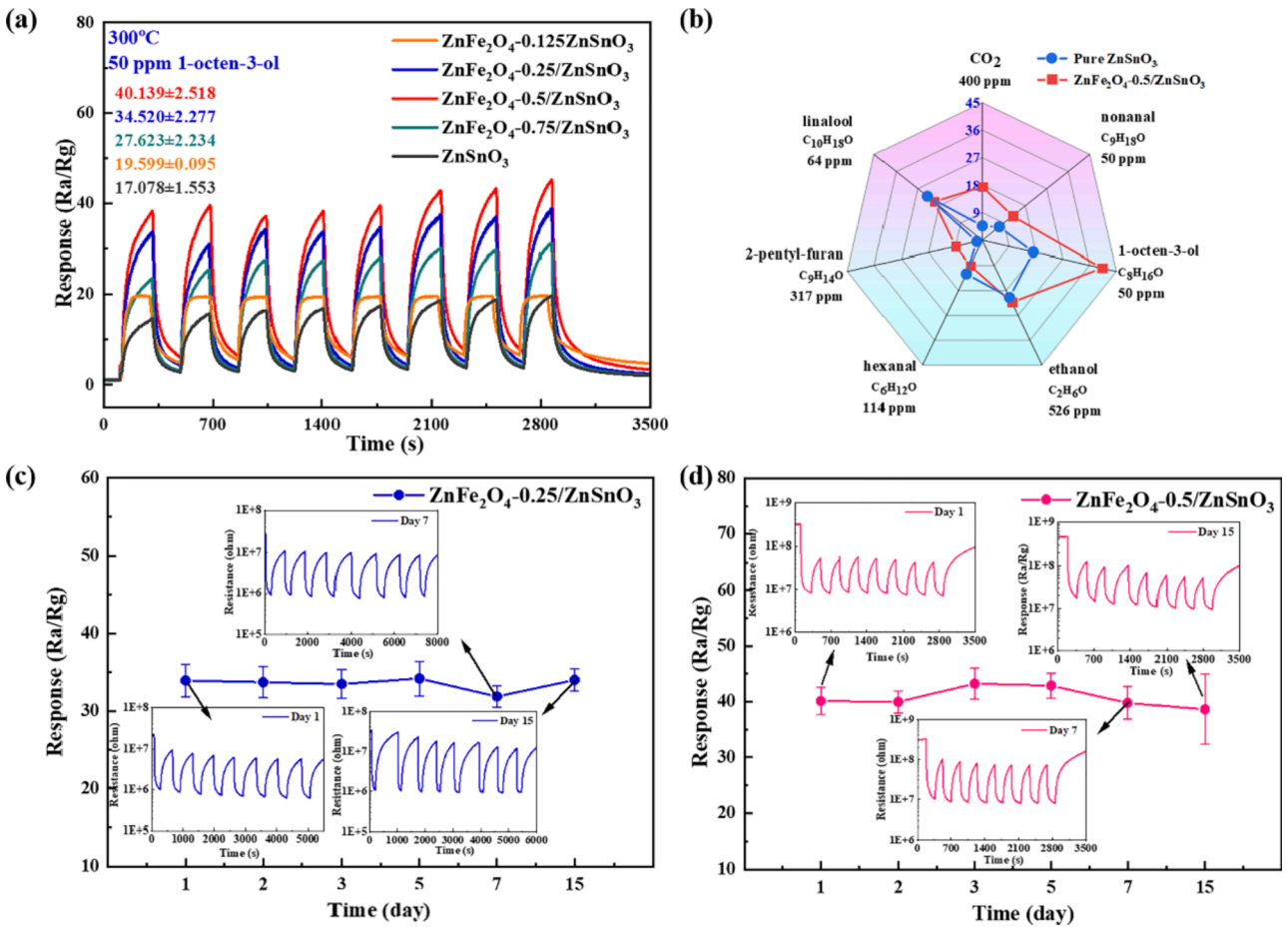

Fig. 8. (a) Repeatable characteristics of pure $ZnSnO_3$ and composites in 8 consecutive responses. (b) Radar chart of gas responses of pure $ZnSnO_3$ (blue lines) and optimum $ZnFe_2O_4$-0.5/$ZnSnO_3$ (red lines) sensors to various common gases during rice mildew at 300 °C. (c-d) Long-term stability (15 days) of $ZnFe_2O_4$-0.25/$ZnSnO_3$ and $ZnFe_2O_4$-0.5/$ZnSnO_3$ based sensor to 50 ppm 1-octen-3-ol at 300 °C. The error bars represent the standard deviations of eight repeated test results.

nanoclusters, of which the maximum response towards 500 ppm 1-octen-3-ol at the optimal working temperature of 300 °C was around 3.3 times superior to that of pristine $ZnSnO_3$. The error bars in Fig. 6c were related to the repeated responses exhibited in Fig. S11a and S11b. It is interesting to note that the reference resistance exhibited a tendency to increase at operating temperatures above 200 °C due to the strong oxygen adsorption on the sensor surface. While in the region above 300 °C, the resistance is not significantly impacted by temperature changes, which may be due to the balance between thermal excitation of electrons and oxygen adsorption. When the temperature reaches 400 °C, the resistance decreases dramatically, resulting from the predominance of electron thermal excitation and oxygen desorption [51]. Therefore, 300 °C was selected as the optimal working temperature for subsequent experiments. Fig. 6d and e present the responses of pure $ZnSnO_3$ and ZFO/ZS composites based sensors to continuous rise of 1-octen-3-ol concentrations ranging from 500 ppm to 20 ppm. All samples were fittingly demonstrated as *n*-type semiconductors on account of the immediate decrease of the resistance once 1-octen-3-ol bubbled into test chamber. The response values linearly varied between 500 and 100 ppm and 100–20 ppm. It can be intuitively observed that the ZFO-0.5/ZS showed the best response signature to 1-octen-3-ol molecules ahead of the other four sensors, and all the composites appeared to have higher response values than pure $ZnSnO_3$. The response to 500 ppm 1-octen-3-ol has already been increased by 1.8 as the loading amount was slightly changed from 0 to 0.125. These results could be primarily ascribed to the increased concentrations of oxygen vacancies and larger specific surface areas, tally with the XPS and BET analysis. Besides, the reference resistances gradually rose as the load amount increased, which were all higher than pure $ZnSnO_3$, probably resulting from the $ZnFe_2O_4$ layers constructed on the $ZnSnO_3$ surface and higher porosity of composites [52–54]. As a result, increased oxygen ions adsorbed on the ZFO-0.5/ZS surface accompanied by lowered carrier concentrations when stabilized in air, which will bring about a larger change in carrier concentration, that is, the drop in resistance after contact with the targeted gas (Fig. S10). As reported in Fig. 6d, recovery conditions of the initial baseline signals after the analyte molecules desorption were less than complete recovery, possibly because of the high polarity of alcohols and strongest interactions between measured gas and sensing materials [55]. It is not hard to see that the response values were not saturated throughout the detection concentration range, suggesting that as-fabricated sensors had the potential to be applied to a much broader detection scope from a few hundred ppb to several percent. In order to gain insight into response and recovery times of ZFO-0.5/ZS based sensor utilizing thermo excitation (300 °C), the transient responses of 20–100 ppm 1-octen-3-ol were studied as plotted in Fig. 6f (detailed information in Fig. S11). The fastest response speed was observed at 100 ppm, due to the increased number of targeted gas molecules encouraging their adsorption on the surface of sensing materials and reaction with oxygen ions. While the recovery times for the mentioned concentrations appeared to have an overall upward trend and exceeded response time at 100 ppm, which was possibly determined by the intense chemical connection between 1-octen-3-ol gas and sensor's surface according to the adsorption and desorption kinetics of gas molecules. Compared to the other four samples, the narrow bandgap, large specific surface area and elevated level of O_{vac} and O_{che} contributed to an optimal combination of outstanding readout response (315/500 ppm)

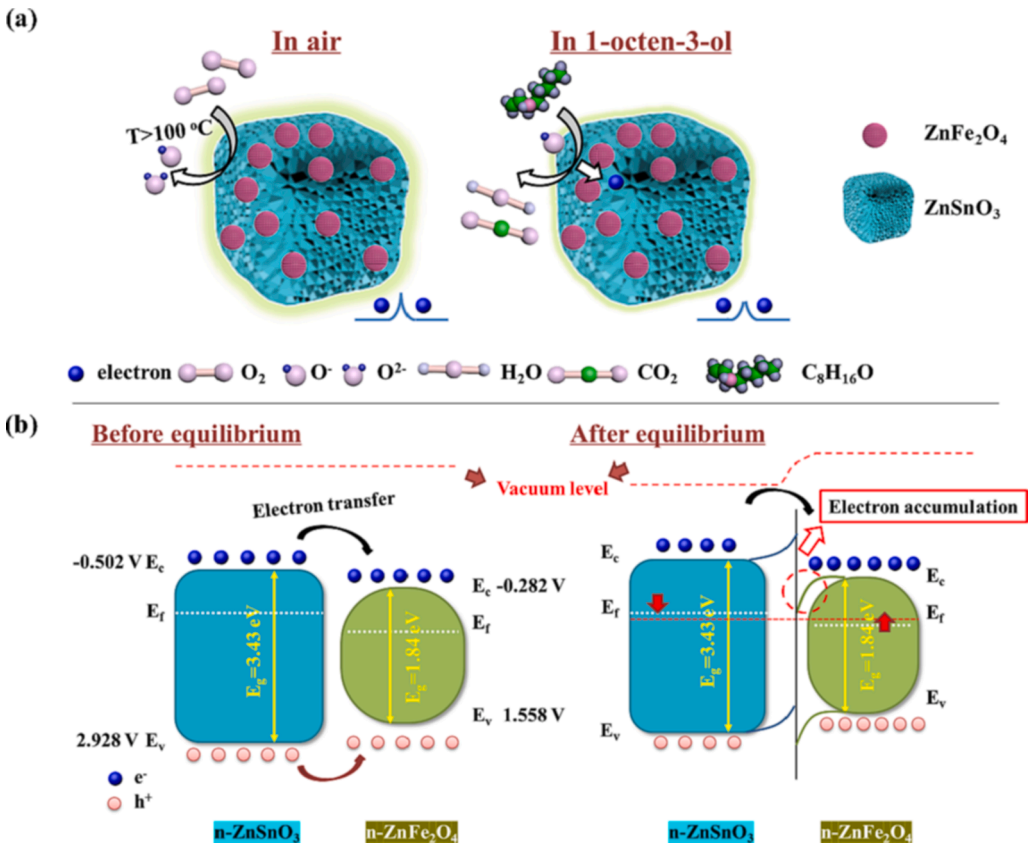

Fig. 9. (a) Schematic illustration of the gas-sensing mechanism of ZFO/ZS based sensor for detecting 1-octen-3-ol. (b) Energy band structure of ZFO/ZS composite.

and relatively short τ_{res} (136.27 s/20 ppm) and τ_{rec} (124.12 s/20 ppm) in ZFO-0.5/ZS heterojunction material.

To explore the sensing performance of ZFO-0.5/ZS in more detail, the dynamic resistance and response in the range of 70–20 ppm have been provided in Fig. S11c. The response values varied with 1-octen-3-ol concentrations in an almost linear fashion ($R^2 = 0.987$ fitted in Fig. S13) and emerged a response surpassing 20 at the detection condition of 20 ppm. Furthermore, we carried out the detection of 1-octen-3-ol concentrations as low as possible if the experimental conditions permit. In addition to the excellent sensing performance for high concentration 1-octen-3-ol of 500 to 20 ppm, ZFO-0.5/ZS composite showed the best response and recovery at low concentrations (8 to 1 ppm) with good baseline stability, indicating favorable real-time repeatability, of which the response values enhanced by factors of 2.18, 2.26, 2.30, 2.29, 2.17, 2.02, 1.76, and 1.61 for on-going targeted gas flow in contrast to pure $ZnSnO_3$ (Fig. 7a and S12d). Besides, 1 ppm 1-octen-3-ol gas could be stably monitored by all samples, and their response values were remarkably correlated linearly with the rising concentrations, as shown in Fig. 7b. The theoretical LOD of 1-octen-3-ol for ZFO/ZS based sensors was demonstrated to be less than 2.42 ppm, and even ppb level for ZFO-0.25/ZS and ZFO-0.5/ZS via the definition Equation (1) and (2) as follows [56,57].

$$LOD(ppm) = \frac{3 \times RMS_{noise}}{k} \quad (1)$$

$$RMS_{noise} = \sqrt{\frac{\sum (y - y_i)^2}{N}} \quad (2)$$

The RMS_{noise} was calculated based on 100 baseline resistance points of corresponding samples, and k was defined as the slope of linear fitting curves in Fig. 7b, of which the concrete data was provided in Table S4. The LOD of pure $ZnSnO_3$ and ZFO-0.5/ZS was 2.77 ppm and 420 ppb, respectively, with a difference of 6.6 times, both much lower than reported in previous literature [7]. It was clear that the formation of *n-n* heterojunction improved the response value of sensors, but the ZFO-0.75/ZS was recorded a relatively high baseline resistance with fluctuations, which resulted in higher RMS_{noise} and LOD. Additionally, sensitivity (η) as an important issue in gas sensor application was also explored in Fig. S14. The η for ZFO-0.5/ZS and ZFO-0.25/ZS attained the highest value of 0.59 through power law equation [58]. Besides, as shown in Fig. S15, the response threshold range of the ZFO-0.5/ZS sensor was tested to be 495.365 for 986.8 ppm and 1.569 for as low as 500 ppb. To sum up, ZFO-0.5/ZS based sensor performed well with excellent reactivity over a wide range of 1-octen-3-ol concentrations. Good sensitivity was achieved at even very low concentrations that reached ppb-level.

The influence of humidity is also an important research link in the uncontrolled practical environment. Fig. 7c exhibits a series of RH ranging from 20 % to 90 % toward 50 ppm 1-octen-3-ol at 300 °C. The response value of ZFO-0.5/ZS decreased to 6.2 once the RH reached 20 %, while when it exceeded 60 %RH, the variation of response shrunken. Under a high-humidity atmosphere of 90 %RH, the response of ZFO-0.5/ZS heterostructure still reached 2, whereas the $ZnSnO_3$ was almost unresponsive. The degraded sensing performance may be attributed to the well-developed pore structure of all samples, providing abundant active sites for adsorbing water molecules. Besides, the water vapor generated in high temperatures gathered to form nanoscale water-rich regions at sensing materials interfaces contributed to impedance features [59]. The decrease of reference resistances conformed to the phenomenon that more electrons returned to the materials after the reaction of water molecules with pre-adsorbed oxygen ions. Fig. 7d displays the dynamic response curve of the ZFO-0.5/ZS based sensor towards various RH, which was continuously exposed to 20 ppm 1-octen-3-ol, demonstrating that the material was very insensitive to humidity changes (highest response value was less than 1.75) with the fluctuation of only 0.0449.

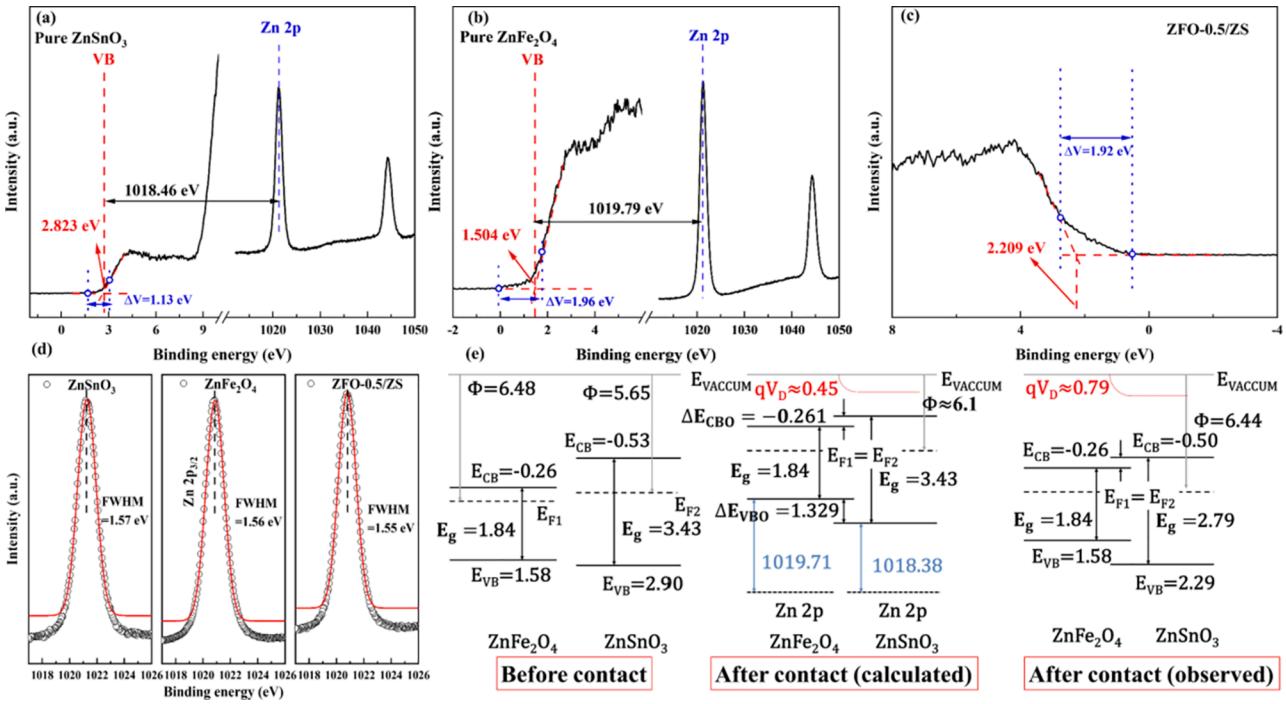

Fig. 10. The XPS core-level and valence band spetra of (a) $ZnSnO_3$, (b) $ZnFe_2O_4$, and (c) ZFO-0.5/ZS. (d) The comparison of high-resolution XPS of Zn $2p_{3/2}$ of three samples. (e) Band alignment of ZFO/ZS heterojunction, where E_{VACUUM} is the vacuum energy level, qV_D is an interface dipole barrier vacuum levels of $ZnFe_2O_4$ and $ZnSnO_3$, the meanings of other symbols were shown in Table S6. The CB and VB values of observed band alignment of ZFO/ZS were considered for $ZnSnO_3$ to simplify the system due to the complexity of separating individual values.

The response values of all samples remained relatively stable in 8 cycles in case of 50 ppm 1-octen-3-ol as evident in Fig. 8a, among which the response of ZFO-0.5/ZS was 40.139 ± 2.518, indicating that the ZFO/ZS based sensors had low repeatable errors, and their response showed no downward trend after repetition. Moreover, analyte selectivity is a key concern for the design of practical sensors. In Fig. 8b, typical VOCs generated in the mildew process of unhusked rice were used as detection objects (the usual ratios under mildew conditions were provided in Table S5). We can observe that the sensitivity of pure $ZnSnO_3$ to linalool is the highest, followed by 1-octen-3-ol and ethanol. Such phenomenon may be due to the increased number of hydrocarbon chain of alcohol, which demonstrated abundant chemisorbed oxygen ions on the material surface, as reported in previous literature [51,60]. However, the selective nature of low-sized mesoporous ZFO-0.5/ZS to 1-octen-3-ol was the best that superior to linalool, possibly attributed to Knudsen diffusion that the diffusion coefficient is inversely proportional to molar mass (M), which means the lighter gas molecules naturally diffuse deeper into sensing layer than heavier ones [61]. Therefore, the load of $ZnFe_2O_4$ significantly improved the selective response to 1-octen-3-ol. To our knowledge, the molar masses of 1-octen-3-ol and linalool are 128.21 g·mol^{-1} and 154.25 g·mol^{-1}. Further tests indicated that our sensors possessed long-term stability under 50 ppm 1-octen-3-ol, which were explored through 8 repeated cycles within 15 days. Fig. 8c and 8d exhibit that the response values of ZFO-0.25/ZS and ZFO-0.5/ZS based sensors with better sensing performance maintained at steady levels at 33.543 ± 0.776 and 40.786 ± 1.693 respectively. The fabricated sensors were stored in a normal laboratory environment without any additional processing.

3.3. Gas sensing mechanism

The sensing mechanism based on microstructure and composition of ZFO/ZS heterostructure has been proposed as follows.

The space-charge layer model was widely used for *n*-type semiconductor sensors (Fig. 9). Various surface absorbed oxygen species (O_2^-, O^-, O^{2-}) formed according to the operating temperature when the materials exposed to air, which trapped free electrons from conduction band and thickened electron depletion layer, finally increased the sensors' resistance. After passing through the target gas, the redox reaction between 1-octen-3-ol molecules and pre-chemisorbed oxygen species released the captured electrons back to the conduction band, which increased the carrier density and lowered the Schottky barrier, thus decreasing the resistance. It follows that the number of absorbed oxygen species has a significant impact on the sensors' sensing performance, and increased electrons contribute to forming more oxygen ions. In Fig. S16a, the smaller Nyquist arc radius indicated faster charge transfer at the interface of ZFO/ZS with higher charge separation capability, and the ZFO-0.5/ZS sample was demonstrated to possess the lowest interfacial charge transfer resistance, corresponding to the sharp variation of resistance change as presented in Fig. S10.

The surface properties of mesoporous structure with high specific surface area and rich O_{vac} and O_{che} enhanced the sensing performance. As seen in Fig. S7, the lattice fringes of $ZnSnO_3$ and $ZnFe_2O_4$ can be clearly staggered, and the distinguished interface observed between two phases further demonstrated the intimate contact between two materials and the construction of heterojunction. Higher interface area contributes to the enhanced sensing performance. The construction of heterojunction significantly increased the concentration of oxygen vacancies, which generated unpaired electrons that served as donors, accompanied by the formation of O_{che}. The presence of O_{vac} makes the charge density near the top of valence band and bottom of conduction band increase significantly, which narrowed the bandgap of materials (Fig. 5a), conducive to the adsorption of tested gas and promotes the removal of thermal electrons. Besides, the hollow nanocubes with nanoparticle-assembled structure endowed the ZFO-0.5/ZS sample high specific surface area, providing more channels for gas molecules' transmission and diffusion, and contributing to the addition of accessible active adsorption sites, which simplified redox reactions with 1-octen-3-ol gas.

Ascending operating temperature boosted the number of thermally excited electrons from the valence band and enhanced the electron

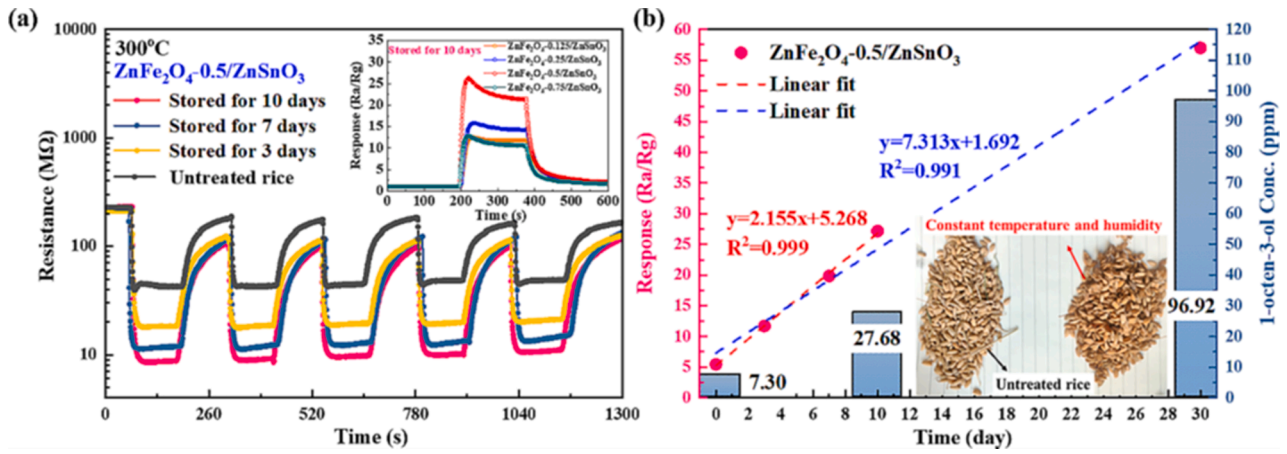

Fig. 11. (a) Resistance curves of $ZnFe_2O_4$-(0.125, 0.25, 0.5, 0.75)/$ZnSnO_3$ based sensors to the volatiles from 50 g unhusked rice after storage for different times in 5 consecutive responses. Inset: response curves of different composite samples for unhusked rice stored for 10 days. (b) Responses of the $ZnFe_2O_4$-0.5/$ZnSnO_3$ sensor as a function of storage time measured at 300 °C under exposure to odors from 50 g unhusked rice (left y axis) and the corresponding released 1-octen-3-ol concentration (right y axis).

mobility and reaction kinetics, which compensated the energy barrier and caused the electron donor to get closer with the narrowed energy gap at thermal excitation. Thermally excited electrons contributed to the efficient injection of $ZnFe_2O_4$ from the CB of $ZnSnO_3$, which then participated in the surface redox reaction, finally improving the sensing performance. This phenomenon illustrated the surface sensing process can be utilized to modulate the electronic properties of the composites.

The establishment of *n-n* type heterostructure positively affected gas sensing performance. It can be seen from the Mott-Schottky curves in Fig. S16b that all the slopes were positive, indicating that the pure $ZnSnO_3$, $ZnFe_2O_4$ and their composites are *n*-type semiconductors. The flat band potential (E_{FB}) values were roughly obtained via extending the linear section to Y-coordinate equal to 0. The calculated VB and CB values were presented in Table S7, which suggested that a straddling type *n-n* isotype heterojunction was created. In addition, the CB of pure $ZnSnO_3$ and $ZnFe_2O_4$ was calculated to be −0.527 eV and −0.256 eV from the VB-XPS spectra in Fig. 10, which were close to the results of Mott-Schottky plot (−0.502 eV and −0.282 eV), further demonstrating the accuracy of the band structure (Table S6). The calculated values of ΔE_{VBO} and ΔE_{CBO} were positive through formulas in Table S6 demonstrating that a type-I band alignment was indeed formed in ZFO/ZS composites after contact. As shown in Fig. 10e, the lower work function of $ZnSnO_3$ implied that the electrons were transferred from the CB of $ZnSnO_3$ to that of $ZnFe_2O_4$, resulting in the respective energy bands of $ZnFe_2O_4$ and $ZnSnO_3$ moving up and down accompanied with the rise of potential energy surface at the interface. The band bending correction caused an interface dipole barrier of ~0.45 eV with a vacuum level of $ZnSnO_3$ below that of $ZnFe_2O_4$. Notably, the experimentally determined band alignment of ZFO/ZS ($\phi = 6.44$ eV) is slightly different than the theoretically calculated ZFO/ZS ($\phi \approx 6.1$ eV), probably resulting from the defect-states such as O_{vac} increasing in one material of the composite and decreasing in other, of which the competition changes the work function. Besides, the CB and VB of $ZnSnO_3$ are shifted toward the E_F, which increases the fast charge transfer from $ZnSnO_3$ to $ZnFe_2O_4$. Besides, the relationship between the heterojunction barrier height and the resistance based on the semiconductor theory defined as $R \propto \exp\left(\frac{qV}{K_0T}\right)$, the exponential relation means that a small variation in the interface dipole barrier will result in a marked difference in the conductivity of the materials. Therefore, when the adsorption and desorption behavior of 1-octen-3-ol occurs, the barrier change of the composite with larger $qV(\approx 0.79eV)$ is more significant accompanied by a higher response value. Fig. 9b exhibited that a depletion region is formed at the interface of two materials with the appearance of a triangular potential well equipped with discrete electron energies. As the electrons keep moving from the CB of $ZnSnO_3$ to the potential well, the electron accumulation occurs and free electrons of heterostructure are trapped in the potential well, accompanied by the increase in overall reference resistance that corresponds to the above gas sensing experiment. Higher reference resistance in turn contributes to the amplitude of variation in resistance when the heterostructure is exposed to the target gas. Additionally, the developed electron reservoir formed via potential well provides abundant electrons for oxygen surface chemisorption and accelerates their conversion to reactive oxygen species, which conforms to the XPS results, thus enhancing the sensing performance.

Density functional theory (DFT) calculation was used further to verify the proposed enhanced mechanism of sensing materials. The surface work functions of the $ZnSnO_3$ (0 0 1) and $ZnFe_2O_4$ (1 1 1) planes were calculated to be 6.504 eV and 8.898 eV by DMol 3, suggesting that the electrons are inclined to transfer from $ZnSnO_3$ to $ZnFe_2O_4$, which contributes to an increased concentration of electrons in outer layers of the composites and more adsorbed oxygen species (Fig. S17). Besides, Fig. S17c displays slightly different energy band structures of $ZnSnO_3$ and $ZnFe_2O_4$ from the experimental UV–vis results through CASTEP calculation for the commonly underestimating band gaps of GGA functional. It can be observed that the formation of heterostructure increases the DOS at the edge of the CB, which promotes the migration of carriers, and then enhances the sensing properties of ZFO/ZS.

3.4. Rice mildew detection

The practical application potential of the proposed sensors was explored by detecting the VOCs emitted from unhusked rice, which had been stored in the granary for 3 months before the following experiment. It has been reported that the quality of newly harvested rice will deteriorate after storage for more than 3 months, and the concentration of 1-octen-3-ol will increase with time go on [1,62]. We carried out early mildew detection on the unhusked rice to verify the practicability of as-fabricated sensors. The rice which had been stored naturally for 3 months was treated for another 3, 7, 10 and 30 days (stored in artificially controlled 50 °C, 90 % RH), and then we detected the 1-octen-3-ol released from it. As shown in Fig. 11a, the ZFO-0.5/ZS showed an enhanced response from 5.434 to 27.164 accompanied by the prolonged storage duration. It can be observed that the sensor can return to the reference resistance after the end of the five cycles, indicating excellent repeatability in practical application. Besides, the ZFO-0.5/ZS based sensor was still significantly better than others, with a response value 1.65 times higher than ZFO-0.25/ZS. Fig. 11b exhibited excellent

linearity with $R^2 = 0.999$ in the first ten days and slightly descending linearity with $R^2 = 0.991$ when the storage time reached one month (Fig. S18). Theoretical response values to the corresponding 1-octen-3-ol gas concentration were also calculated from Figs. 7b and S11 In addition, after 30 days of storage at constant temperature and humidity, rice showed the characteristic phenomenon of early mildew that color darkened, as shown in the inset picture in Fig. 11b. Hence, the as-fabricated sensors have been proved to be highly sensitive to the change of mildew smell of unhusked rice during different storage periods, which possesses the promising potential for 1-octen-3-ol detection and early mildew monitoring in rice.

4. Conclusion

In summary, a facile-synthesized and reliable 1-octen-3-ol sensor was created based on ZFO/ZS heterostructure. Compared with pristine $ZnSnO_3$, the composite sensors presented outstanding responses toward 1–500 ppm 1-octen-3-ol, with high sensitivity, good selectivity, low limit of detection (420 ppb), and excellent repeatability and long-term stability. The decreased grain size, abundant oxygen defects, high specific area and increased charge separation capability of the fine-tuned ZFO/ZS with the formation of numerous heterojunction interfaces contribute to the enhanced sensing properties. Besides, the as-prepared sensors were applied in VOCs detection of unhusked rice to demonstrate the practical application potential in rice mildew evaluation. Future work will focus on the multiple integrations of ZFO/ZS heterostructured composite with other sensing materials on a platform to distinguish diverse characterized VOCs released from unhusk rice and realize comprehensive qualitative and quantitative evaluation to analyze rice mildew accurately. Therefore, the as-fabricated sensors reported here have a high potential for use as practical gas-sensing devices for 1-octen-3-ol, which are anticipated to be extended to other agriculture products detection for quality and safety evaluation.

Declaration of Competing Interest

The authors declare that they have no known competing financial interests or personal relationships that could have appeared to influence the work reported in this paper.

Data availability

Data will be made available on request.

Acknowledgments

This work is supported by the National Natural Science Foundation of China under Grant No. 51872254, the Outstanding Youth Foundation of Jiangsu Province of China under Grant No. BK20211548, the National Key Research and Development Program of China under Grant No. 2017YFE0115900 and Graduate Research Innovation Program of Jiangsu Province of China under Grant No. KYCX22_3494.

Appendix A. Supplementary data

Supplementary data to this article can be found online at https://doi.org/10.1016/j.cej.2022.139824.

References

[1] K. Liu, C. Zhang, J. Xu, Q. Liu, Research advance in gas detection of volatile organic compounds released in rice quality deterioration process, Compr. Rev. Food. Sci. Food. Saf. 20 (2021) 5802–5828, https://doi.org/10.1111/1541-4337.12846.
[2] Z. Zheng, C. Zhang, Electronic noses based on metal oxide semiconductor sensors for detecting crop diseases and insect pests, Comput. Electron. Agric. 197 (2022), 106988, https://doi.org/10.1016/j.compag.2022.106988.
[3] Z. Zheng, K. Liu, K. Xu, C. Zhang, Investigation on microstructure and nonanal sensing properties of hierarchical Sb_2WO_6 microspheres, Ceram. Int. (2022), https://doi.org/10.1016/j.ceramint.2022.06.298.
[4] S. Sen, R. Chakraborty, P. Kalita, Rice - not just a staple food: A comprehensive review on its phytochemicals and therapeutic potential, Trends Food Sci. Technol. 97 (2020) 265–285, https://doi.org/10.1016/j.tifs.2020.01.022.
[5] R. Kataoka, T. Watanabe, S. Yano, O. Mizutani, O. Yamada, T. Kasumi, J. Ogihara, Aspergillus luchuensis fatty acid oxygenase ppoC is necessary for 1-octen-3-ol biosynthesis in rice koji, J. Biosci. Bioeng. 129 (2020) 192–198, https://doi.org/10.1016/j.jbiosc.2019.08.010.
[6] F. Brodhun, I. Feussner, Oxylipins in fungi, FEBS J. 278 (2011) 1047–1063, https://doi.org/10.1111/j.1742-4658.2011.08027.x.
[7] L. Shokrzadeh, P. Mohammadi, M.R. Mahmoudian, W.J. Basirun, M. Bahreini, L-glycine-assisted synthesis of SnO_2/Pd nanoparticles and their application in detection of biodeteriorating fungi, Mater. Chem. Phys. 240 (2020), 122172, https://doi.org/10.1016/j.matchemphys.2019.122172.
[8] A.A. Inamdar, J.C. Moore, R.I. Cohen, J.W. Bennett, A model to evaluate the cytotoxicity of the fungal volatile organic compound 1-octen-3-ol in human embryonic stem cells, Mycopathologia 173 (2012) 13–20, https://doi.org/10.1007/s11046-011-9457-z.
[9] X.J. Fan, X. Jiao, J.G. Liu, M. Jia, C. Blanchard, Z.K. Zhou, Characterizing the volatile compounds of different sorghum cultivars by both GC-MS and HS-GC-IMS, Food Res. Int. 140 (2021), 109975, https://doi.org/10.1016/j.foodres.2020.109975.
[10] J.T. Magalhaes, S.M. Barrouin-Melo, A.G. Correa, F. Silva, V.E. Machado, J. S. Govone, M.C. Pinto, A laboratory evaluation of alcohols as attractants for the sandfly Lutzomyia longipalpis (Diptera: Psychodidae), Parasite Vector 7 (2014) 60, https://doi.org/10.1186/1756-3305-7-60.
[11] X.Z. Wang, M.M. Huang, Y. Peng, W.T. Yang, J.Y. Shi, Antifungal activity of 1-octen-3-ol against Monilinia fructicola and its ability in enhancing disease resistance of peach fruit, Food Control 135 (2022), 108804, https://doi.org/10.1016/j.foodcont.2021.108804.
[12] S.U. Morath, R. Hung, J.W. Bennett, Fungal volatile organic compounds: A review with emphasis on their biotechnological potential, Fungal Biol. Rev. 26 (2012) 73–83, https://doi.org/10.1016/j.fbr.2012.07.001.
[13] C. Xie, C.K. Liu, H.L. Loi, F. Yan, Perovskite-based phototransistors and hybrid photodetectors, Adv. Funct. Mater. 30 (2020) 1903907, https://doi.org/10.1002/adfm.201903907.
[14] Q. Sun, W.-J. Yin, Thermodynamic stability trend of cubic perovskites, J. Am. Chem. Soc. 139 (2017) 14905–14908, https://doi.org/10.1021/jacs.7b09379.
[15] J.M. Wu, C.Y. Chen, Y. Zhang, K.H. Chen, Y. Yang, Y.F. Hu, J.H. He, Z.L. Wang, Ultrahigh sensitive piezotronic strain sensors based on a $ZnSnO_3$ nanowire/microwire, ACS Nano 6 (2012) 4369–4374, https://doi.org/10.1021/nn3010558.
[16] J.M. Wu, C. Xu, Y. Zhang, Z.L. Wang, Lead-free nanogenerator made from single $ZnSnO_3$ microbelt, ACS Nano 6 (2012) 4335–4340, https://doi.org/10.1021/nn300951d.
[17] D. Kovacheva, K. Petrov, Preparation of crystalline $ZnSnO_3$ from Li_2SnO_3 by low-temperature ion exchange, Solid State Ionics 109 (1998) 327–332, https://doi.org/10.1016/S0167-2738(97)00507-9.
[18] Y.C. Wang, J.M. Wu, Effect of controlled oxygen vacancy on H-2-production through the piezocatalysis and piezophototronics of ferroelectric R3C $ZnSnO_3$ nanowires, Adv. Funct. Mater. 30 (2020) 1907619, https://doi.org/10.1002/adfm.201907619.
[19] Z.Y. Wang, J.Y. Miao, H.X. Zhang, D. Wang, J.B. Sun, Hollow cubic $ZnSnO_3$ with abundant oxygen vacancies for H_2S gas sensing, J. Hazard. Mater. 391 (2020), 122226, https://doi.org/10.1016/j.jhazmat.2020.122226.
[20] T. Zhou, T. Zhang, R. Zhang, Z. Lou, J. Deng, L. Wang, Hollow $ZnSnO_3$ cubes with controllable shells enabling highly efficient chemical sensing detection of formaldehyde vapors, ACS Appl. Mater. Interfaces 9 (2017) 14525–14533, https://doi.org/10.1021/acsami.7b03112.
[21] B.S. Sá, C.A. Zito, T.M. Perfecto, D.P. Volanti, Porous $ZnSnO_3$ nanocubes as a triethylamine sensor, Sensors Actuators B: Chem. 338 (2021) 129869.
[22] P.F. Cheng, L. Lv, Y.L. Wang, Y. Zhang, Y.Q. Zhang, Z.H. Lei, L.P. Xu, SnO_2/$ZnSnO_3$ double-shelled hollow microspheres based high-performance acetone gas sensor. Sen. Actuators, B 332 (2021) 129212, 10.1016/j.snb.2020.129212.
[23] X.Y. Wang, Y.P. Liu, B.N. Ding, H. Li, X.T. Zhu, M.Z. Xia, H. Fu, Influence of the addition of nano-TiO_2 and ZnO on the sensing performance of micro-$ZnSnO_3$ ethanol sensors under UV illumination, Sen. Actuators B 276 (2018) 211–221, https://doi.org/10.1016/j.snb.2018.08.114.
[24] X.Y. Wang, B.N. Ding, Y.P. Liu, X.T. Zhu, H. Li, M.Z. Xia, H. Fu, M.X. Li, Synthesis of 3D flower-like $ZnSnO_3$ and improvement of ethanol-sensing properties at room temperature based on nano-TiO_2 decoration and UV radiation, Sen. Actuators B 264 (2018) 119–127, https://doi.org/10.1016/j.snb.2018.02.178.
[25] S.L. Bai, Y. Tian, Y.H. Zhao, H. Fu, P.G. Tang, R.X. Luo, D.Q. Li, A.F. Chen, C.C. Liu, Construction of NiO@$ZnSnO_3$ hierarchical microspheres decorated with NiO nanosheets for formaldehyde sensing, Sen. Actuators, B 259 (2018) 908–916, https://doi.org/10.1016/j.snb.2017.10.176.
[26] W. Guo, L. Huang, B. Zhao, X. Gao, Z. Fan, X. Liu, Y. He, J. Zhang, Synthesis of the $ZnFe_2O_4$/$ZnSnO_3$ nanocomposite and enhanced gas sensing performance to acetone, Sens. Actuators, B 346 (2021), 130524, https://doi.org/10.1016/j.snb.2021.130524.
[27] H.-M. Fan, J.-B. Yi, Y. Yang, K.-W. Kho, H.-R. Tan, Z.-X. Shen, J. Ding, X.-W. Sun, M.C. Olivo, Y.-P. Feng, Single-crystalline MFe_2O_4 nanotubes/nanorings synthesized by thermal transformation process for biological applications, ACS Nano 3 (2009) 2798–2808, https://doi.org/10.1021/nn9006797.

[28] A. Šutka, K.A. Gross, Spinel ferrite oxide semiconductor gas sensors, Sens. Actuators, B 222 (2016) 95–105, https://doi.org/10.1016/j.snb.2015.08.027.
[29] N. Van Hoang, C.M. Hung, N.D. Hoa, N. Van Duy, N. Van Hieu, Facile on-chip electrospinning of $ZnFe_2O_4$ nanofiber sensors with excellent sensing performance to H_2S down ppb level, J. Hazard. Mater. 360 (2018) 6–16, https://doi.org/10.1016/j.jhazmat.2018.07.084.
[30] J.T. Wu, D.J. Gao, T. Sun, J. Bi, Y. Zhao, Z.L. Ning, G.Y. Fan, Z.X. Xie, Highly selective gas sensing properties of partially inversed spinel zinc ferrite towards H_2S, Sen. Actuators, B 235 (2016) 258–262, https://doi.org/10.1016/j.snb.2016.05.083.
[31] N. Van Hoang, C.M. Hung, N.D. Hoa, N. Van Duy, I. Park, N. Van Hieu, Excellent detection of H_2S gas at ppb concentrations using $ZnFe_2O_4$ nanofibers loaded with reduced graphene oxide, Sen. Actuators, B 282 (2019) 876–884, https://doi.org/10.1016/j.snb.2018.11.157.
[32] W. Zhang, Y.B. Shen, J. Zhang, H.S. Bi, S.K. Zhao, P.F. Zhou, C. Han, D.Z. Wei, N. Cheng, Low-temperature H_2S sensing performance of Cu-doped $ZnFe_2O_4$ nanoparticles with spinel structure, Appl. Surf. Sci. 470 (2019) 581–590, https://doi.org/10.1016/j.apsusc.2018.11.164.
[33] W. Guo, L. Huang, X. Liu, J. Wang, J. Zhang, Enhanced isoprene gas sensing performance based on p-$CaFe_2O_4$/n-$ZnFe_2O_4$ heterojunction composites, Sens. Actuators, B 354 (2022), 131243, https://doi.org/10.1016/j.snb.2021.131243.
[34] X. Li, C. Wang, H. Guo, P. Sun, F. Liu, X. Liang, G. Lu, Double-shell architectures of $ZnFe_2O_4$ nanosheets on ZnO hollow spheres for high-performance gas sensors, ACS Appl. Mater. Interfaces 7 (2015) 17811–17818, https://doi.org/10.1021/acsami.5b04118.
[35] C. Zheng, C. Zhang, K. Zhang, J. Zhang, L. Jin, A.M. Asiri, K.A. Alamry, L. He, X. Chu, Growth of $ZnFe_2O_4$ nanosheets on reduced graphene oxide with enhanced ethanol sensing properties. Sens. Actuators, B 330 (2021) 129280, 10.1016/j.snb.2020.129280.
[36] X. Zhou, B.Q. Wang, H.B. Sun, C. Wang, P. Sun, X.W. Li, X.L. Hu, G.Y. Lu, Template-free synthesis of hierarchical $ZnFe_2O_4$ yolk-shell microspheres for high-sensitivity acetone sensors, Nanoscale 8 (2016) 5446–5453, https://doi.org/10.1039/c5nr06308f.
[37] S.N. Hou, P.L. Wang, Y.X. Nie, Y.P. Guo, Q. Ma, A novel work function tuning strategy-based ECL sensor with sulfur dots and Au NP@MoS_2 nanosheet heterostructure for triple-negative breast cancer diagnosis, Chem. Eng. J. 446 (2022), 136906, https://doi.org/10.1016/j.cej.2022.136906.
[38] Q.T.H. Ta, N.M. Tran, N.N. Tri, A. Sreedhar, J.S. Noh, Highly surface-active Si-doped TiO_2/$Ti_3C_2T_x$ heterostructure for gas sensing and photodegradation of toxic matters, Chem. Eng. J. 425 (2021), 131437, https://doi.org/10.1016/j.cej.2021.131437.
[39] C. Balamurugan, K. Cho, B. Park, J. Kim, N. Kim, Y. Pak, J. Kong, S. Kwon, Large modulation of the chemical and electronic sensitization of TiO_2/Ag/NiO nanostructure via in situ hydrothermal-induced heterointerface engineering, Chem. Eng. J. 430 (2022), 132690, https://doi.org/10.1016/j.cej.2021.132690.
[40] M. Miyauchi, Z.F. Liu, Z.G. Zhao, S. Anandan, K. Hara, Single crystalline zinc stannate nanoparticles for efficient photo-electrochemical devices, Chem. Commun. 46 (2010) 1529–1531, https://doi.org/10.1039/b921010e.
[41] M. Su, C. He, V.K. Sharma, M. Abou Asi, D. Xia, X.-Z. Li, H. Deng, Y. Xiong, Mesoporous zinc ferrite: synthesis, characterization, and photocatalytic activity with H_2O_2/visible light, J. Hazard. Mater. 211–212 (2012) 95–103, https://doi.org/10.1016/j.jhazmat.2011.10.006.
[42] J. Li, M. Yang, Y. Li, X. Cheng, X. Zhang, Y. Xu, S. Gao, H. Zhao, L. Huo, Construction of SnO_2 nanoneural network by ultrasmall particles for highly selective NO_2 detection at low temperature, Sens. Actuators B 361 (2022), 131703, https://doi.org/10.1016/j.snb.2022.131703.
[43] S. Li, Y.C. Zhang, L. Han, X.L. Li, Y. Xu, Hierarchical kiwifruit-like ZnO/$ZnFe_2O_4$ heterostructure for high-sensitive triethylamine gaseous sensor, Sen. Actuators, B 344 (2021), 130251, https://doi.org/10.1016/j.snb.2021.130251.
[44] C. Zhang, G.F. Liu, K.W. Liu, K.D. Wu, ZnO_{1-x} coatings deposited by atmospheric plasma spraying for room temperature ppb-level NO_2 detection, Appl. Surf. Sci. 528 (2020), 147041, https://doi.org/10.1016/j.apsusc.2020.147041.
[45] J. Huang, X. Xu, C. Gu, W. Wang, B. Geng, Y. Sun, J. Liu, Size-controlled synthesis of porous $ZnSnO_3$ cubes and their gas-sensing and photocatalysis properties, Sens. Actuators B 171–172 (2012) 572–579, https://doi.org/10.1016/j.snb.2012.05.036.
[46] B.S. Surendra, H.P. Nagaswarupa, M.U. Hemashree, J. Khanum, Jatropha extract mediated synthesis of $ZnFe_2O_4$ nanopowder: Excellent performance as an electrochemical sensor, UV photocatalyst and an antibacterial activity, Chem. Phys. Lett. 739 (2020), 136980, https://doi.org/10.1016/j.cplett.2019.136980.
[47] Y. Chen, L. Yu, Q. Li, Y. Wu, Q. Li, T. Wang, An evolution from 3D face-centered-cubic $ZnSnO_3$ nanocubes to 2D orthorhombic $ZnSnO_3$ nanosheets with excellent gas sensing performance, Nanotechnology 23 (2012), 415501, https://doi.org/10.1088/0957-4484/23/41/415501.
[48] S. Yang, Z. Han, F. Zheng, J. Sun, Z. Qiao, X. Yang, L. Li, C. Li, X. Song, B. Cao, $ZnFe_2O_4$ nanoparticles-cotton derived hierarchical porous active carbon fibers for high rate-capability supercapacitor electrodes, Carbon 134 (2018) 15–21, https://doi.org/10.1016/j.carbon.2018.03.071.
[49] K. Wu, M. Debliquy, C. Zhang, Room temperature gas sensors based on Ce doped $TiO_{.2}$ nanocrystals for highly sensitive NH_3 detection, Chem. Eng. J. 444 (2022), 136449, https://doi.org/10.1016/j.cej.2022.136449.
[50] J. Ma, H. Fan, X. Zheng, H. Wang, N. Zhao, M. Zhang, A.K. Yadav, W. Wang, W. Dong, S. Wang, Facile metal-organic frameworks-templated fabrication of hollow indium oxide microstructures for chlorine detection at low temperature, J. Hazard. Mater. 387 (2020), 122017, https://doi.org/10.1016/j.jhazmat.2020.122017.
[51] N.H. Al-Hardan, M.J. Abdullah, A.A. Aziz, H. Ahmad, L.Y. Low, ZnO thin films for VOC sensing applications, Vacuu. 85 (2010) 101–106, https://doi.org/10.1016/j.vacuum.2010.04.009.
[52] M.H. Seo, M. Yuasa, T. Kida, J.S. Huh, K. Shimanoe, N. Yamazoe, Gas sensing characteristics and porosity control of nanostructured films composed of TiO_2 nanotubes, Sen. Actuators, B 137 (2009) 513–520, https://doi.org/10.1016/j.snb.2009.01.057.
[53] X. Zhu, X. Chang, S. Tang, X. Chen, W. Gao, S. Niu, J. Li, Y. Jiang, S. Sun, Humidity-tolerant chemiresistive gas sensors based on hydrophobic CeO_2/SnO_2 heterostructure films, ACS Appl. Mater. Interfaces 14 (2022) 25680–25692, https://doi.org/10.1021/acsami.2c03575.
[54] K. Zhang, S.W. Qin, P.G. Tang, Y.J. Feng, D.Q. Li, Ultra-sensitive ethanol gas sensors based on nanosheet-assembled hierarchical ZnO-In_2O_3 heterostructures, J. Hazard. Mater. 391 (2020), 122191, https://doi.org/10.1016/j.jhazmat.2020.122191.
[55] M. Consales, A. Crescitelli, M. Penza, P. Aversa, P.D. Veneri, M. Giordano, A. Cusano, SWCNT nano-composite optical sensors for VOC and gas trace detection, Sen. Actuators, B 138 (2009) 351–361, https://doi.org/10.1016/j.snb.2009.02.041.
[56] P. Clement, S. Korom, C. Struzzi, E.J. Parra, C. Bittencourt, P. Ballester, E. Llobet, Deep cavitand self-assembled on Au NPs-MWCNT as highly sensitive benzene sensing interface, Adv. Funct. Mater. 25 (2015) 4011–4020, https://doi.org/10.1002/adfm.201501234.
[57] W. Zheng, Y.S. Xu, L.L. Zheng, C. Yang, N. Pinna, X.H. Liu, J. Zhang, MoS_2 Van der Waals p-n junctions enabling highly selective room-temperature NO_2 sensor, Adv. Funct. Mater. 30 (2020) 2000435, https://doi.org/10.1002/adfm.202000435.
[58] S. Acharyya, S. Nag, S. Kimbahune, A. Ghose, A. Pal, P.K. Guha, Selective discrimination of VOCs applying gas sensing kinetic analysis over a metal oxide-based chemiresistive gas sensor, ACS Sens. 6 (2021) 2218–2224, https://doi.org/10.1021/acssensors.1c00115.
[59] M.T. Robinson, J.L. Tung, M.H. Gharahcheshmeh, K.K. Gleason, Humidity-initiated gas sensors for volatile organic compounds sensing, Adv. Funct. Mater. 31 (2021) 2101310, https://doi.org/10.1002/adfm.202101310.
[60] J. Zhao, L.H. Huo, S. Gao, H. Zhao, J.G. Zhao, Alcohols and acetone sensing properties of SnO_2 thin films deposited by dip-coating, Sen. Actuators, B 115 (2006) 460–464, https://doi.org/10.1016/j.snb.2005.10.024.
[61] A. Nandi, P. Nag, H. Saha, S. Majumdar, Precursor dependent morphologies of microwave assisted ZnO nanostructures and their VOC detection properties, Materials Today: Proceedings 5 (2018) 9831–9838, https://doi.org/10.1016/j.matpr.2017.10.174.
[62] T. Chen, C.Y. Liu, L.L. Meng, D.L. Lu, B. Chen, Q.W. Cheng, Early warning of rice mildew based on gas chromatography-ion mobility spectrometry technology and chemometrics, J. Food Meas, Charact. 15 (2021) 1939–1948, https://doi.org/10.1007/s11694-020-00775-9.